Active Control of THz Waves in Wireless Environments using Graphene-based RIS

Sasmita Dash, *Member, IEEE*, Constantinos Psomas, *Senior Member, IEEE*, Ioannis Krikidis, *Fellow, IEEE*, Ian F. Akyildiz, *Fellow, IEEE* and Andreas Pitsillides, *Senior Member, IEEE*

***Abstract*—The active and dynamic control of the TeraHertz (THz) waves is highly demanded due to the rapid development of wireless communication systems. Recently, reconfigurable intelligent surface (RIS) has gained significant attention due to their tremendous potential in controlling the electromagnetic waves. Particularly, RIS-based wireless communications are promising for improving the system's performance by properly designing the reflection coefficient of the unit cell. In this work, we investigate a graphene-based RIS for active and dynamic control of THz waves. The RIS design consists of rectangular graphene meta-atoms periodic array placed over a metallic grounded silicon substrate. An equivalent circuit modeling of the RIS design and its solution is provided. The RIS performance is numerically analyzed. The graphene-based RIS achieves nearly 100% reflection in the operational frequency ranging from 0.1 to 4 THz. The perfect reflection is insensitive to the polarization and the incident angles. Moreover, 100% absorption in the graphene-based RIS is achieved by electrically reconfiguring the meta-atom response via the chemical potential of the graphene. The graphene RIS also achieves the anomalous reflection performance by controlling the number of unit cells and phase gradient of RIS. In view of the effective THz wireless communication environment, this paper finally presents a simple RIS-aided communication model to study the impact of the proposed graphene-based RIS on the signal-to-noise ratio. The results reveal that the proposed THz RIS with graphene meta-atoms is promising for efficient and intelligent THz wireless communications.**

***Index Terms*—Wave control, terahertz, reconfigurable intelligent surface, graphene, wireless communications**

I. Introduction

The TeraHertz (THz) spectrum has attracted considerable interest in numerous fields such as spectroscopy, sensing, imaging, communication, biomedical and space applications over the past few years [1]–[4]. The THz band (0.1 - 10 THz) in the electromagnetic spectrum lies between millimeter and far-infrared (IR) band [1]. Recently, the THz spectrum attracted more attention in wireless communications due to the large bandwidth and high data rates. The large bandwidth in the order of THz opens the opportunity to transmit high data rate in the order of terabits per second (Tbps) [2]. In the microwave (MW) band, the high data rate achievement is relatively challenging mainly due to the narrow bandwidth. In addition to this inherent benefit of wide bandwidth, when compared to either MW/millimeter or IR systems, THz wireless communication has other advantages such as (i) more directional than MW/millimeter links, (ii) smaller attenuation than IR, (iii) lower scintillation effects than IR, etc. [5]. Despite the above benefits, THz communications have a couple of challenges. Specifically, the free space path loss is significant in the THz band compared to MW frequencies. Moreover, THz signals experience both spreading and molecular absorption losses. Therefore, THz wireless communications are promising for short-range indoor environments.

The THz band also has a great possibility for future sixth-generation (6G) wireless communication technology. However, in a wireless environment, the emitted electromagnetic (EM) waves undergo attenuation on account of material absorption loss and wave scattering due to the phenomena of reflection, refraction and diffraction, which lead to multiplicity paths of propagation between devices. Thus, the environment is uncontrollable and has a detrimental impact on communications. The attenuation of the signal limits the radius of connectivity and multi-path propagation results in fading phenomena. At MW frequencies, large objects such as walls, floors, ceilings, and doors act as EM wave scatterers, creates multiple paths between communication endpoints. At THz frequencies, small objects even act as substantial scatterers, causing acute signal deterioration. The promising solution for controlled wireless environment is metasurface (MSF).

MSFs are two-dimensional (2D) version of metamaterials. They are thin artificial structures with sub-wavelength meta-atoms (unit cells), which are periodically arranged on a planar surface [6]. Due to their sub-wavelength periodicity, MSFs are characterized by surface material parameters, such as conductivities or impedances. In recent years, MSFs have attracted tremendous attention due to their ability of tailoring the characteristics of EM waves and have open up more possibilities in manipulating the EM characteristics in wave propagation [7]. Depending on the properties of the unit cells, MSFs provide attractive properties and unprecedented control of EM waves [6]. MSFs have potential for the realization of a wide range of EM functions and applications, such as anomalous reflection/transmission [8], [9], perfect absorption [10], polarization control [11], phase control [12], beam splitting [13], wavefront shaping [14], imaging [15], holography [16], energy accumulation [17], wireless power transfer [18], etc. MSFs have gained significant attention for wireless environments due to their wave propagation control ability [19]. Tunable MSFs are realized by incorporating lumped-elements

This work has received funding from the European Research Council (ERC) under the European Union's Horizon 2020 research and innovation programme (Grant agreement No. 819819).

S. Dash, C. Psomas and I. Krikidis are with the Department of Electrical and Computer Engineering, University of Cyprus, Nicosia, Cyprus (e-mail: {dash.sasmita, psomas.constantinos, krikidis.ioannis}@ucy.ac.cy). I. F. Akyildiz and A. Pitsillides are with the Department of Computer Science, University of Cyprus, Nicosia, Cyprus (e-mail: ian.akyildiz@cs.ucy.ac.cy, andreas.pitsillides@ucy.ac.cy)

in the unit cell configuration with appropriate biasing signals. When all unit cells are controlled collectively by modulation of bias voltage, the surface impedance of the MSF is uniformly modified and leading to the tuning of functionality. A reconfigurable/tunable MSF can also be realized electrically, mechanically, optically, thermally, and chemically. The response of a MSF can be switched between perfect absorption and perfect reflection/transmission by controlling the bias voltage. MSF structures are distinguished as either 1-port (reflection) or 2-port (transmission). The complex reflection and transmission coefficients are used to explain their unit-cell response. A reflective MSF can operate as a tunable absorber/reflector [20] and a transmissive MSF is transparent/absorptive [21].

Due to the reconfiguration capability, a tunable MSF is known as reconfigurable intelligent surface (RIS); it is also referred to as intelligent reflecting surface. RIS gained considerable attention to improve wireless networks' capacity and coverage by intelligently reconfiguring the wave propagation of the wireless environment. Henceforth, RIS is promising for the 6G communication networks [22], [23]. In designing RIS-assisted communication systems, the most significant RIS parameter is each unit cell's reflection coefficient. A local or global control over the complex coefficients can lead to several tunable functionalities and related applications, for example, polarizers, absorbers, anomalous reflectors etc.

Many types of MSFs exist in the literature based on their properties [24]. These includes multi-resonance MSF, gap-plasmon MSF, Pancharatnam–Berry-Phase (PB Phase) MSF, Huygens' MSF, all-dielectric Huygens' MSF, and High-Contrast MSF . Reconfigurable/tunable MSFs can be further categorized into several categories based on their approaches, such as electrically tunable MSF, mechanically switchable MSF, optically tunable MSF, thermally tunable MSF, and chemically tunable MSF. For wireless communications, the RIS hardware architecture designs can be classified into three categories [25]: the first is concerned with whether an RIS contains active or passive components, which determines its overall power consumption, the second is based on whether a RIS is a contiguous surface or it consists of discrete elements, and the third is related to the RIS modes of operation in wireless communication system.

Copper is the commonly used metal in MW MSF implementation and switching mechanism technique is normally adopted to achieve reconfigurability. However, the copper material is not suitable for MSF design when the spectrum is extended to the THz band. The conventional metal MSF can lack the adaptability and reconfigurability for THz implementation. Moreover, the introduction of switchable or tunable elements increases complexity in THz MSF design. At THz band, novel nanomaterial graphene has great potential for the design of MSF by exploiting its unique tunable properties. In the last decade, nanomaterial graphene has shown great potential in the design of THz devices. Owing to its novel electronic properties at THz frequencies, the attraction for graphene has increased among the THz research community over the past few years. Due to the conductivity tunability behaviour at THz band, graphene-based devices enable reconfiguration [26]–[28]. The EM propagation in graphene-based devices can be manipulated by dynamically tuning the surface conductivity. Recently, graphene has gained interest in the design of MSF [29]–[31]. Graphene enables intelligent MSF and metamaterial due to the strong optical response of its surface plasmons. With the capability of being electrically tunable, graphene can be a suitable candidate for designing the THz MSF. The MSF design using graphene meta-atom can act as an intelligent environment for THz wireless communications.

In the literature, there are some works that discuss perfect absorption of THz wave by using graphene based nanostructure [30]–[33]. However, the perfect reflection performance of THz wave is not yet reported. For the practical THz wireless communication system, the high reflection efficiency of THz wave is highly desired. In this work, we have designed an efficient perfect THz reflector using a simple structured graphene-based RIS. Besides the perfect reflection properties, graphene-based RIS has the capability to achieve the perfect absorption of THz wave. The potential for wavefront manipulation functionality of the THz RIS, exemplified through anomalous reflection capabilities, is also demonstrated. Moreover, a graphene-based RIS-aided communication model is presented. To the author's knowledge, for the first time, this paper presents THz RIS using graphene meta-atoms as a perfect reflector of the THz waves. The main contributions of this paper are summarized as follows.

- We propose a novel and simple graphene-based RIS design operating at the THz band, which actively manipulates the incoming THz waves. Specifically, the RIS design consists of a rectangular graphene meta-atoms periodic array placed over a metallic grounded silicon substrate. An equivalent circuit modeling of the proposed RIS design and its solution is provided.
- We investigate the performance of the proposed THz RIS by analyzing the graphene meta-atom response. The simple structured graphene THz RIS provides the perfect wideband reflection (nearly 100%) in the operational frequency ranging from 0.1 to 4 THz. The proposed graphene-based RIS is larger insensitive to angle of incidence and angle of polarization. The reflection performance of the graphene RIS is evaluated under the normal and oblique angle of incidences in both transverse electric (TE) and transverse magnetic (TM) polarization. Also, the impact of the dimension of the graphene unit cell on the reflection performance of RIS is studied.
- Furthermore, 100% absorption and anomalous reflection performance of proposed THz RIS are investigated by controlling the chemical potential of the graphene meta-atoms. The capability of dynamically steering the reflection angle in a wide range by controlling the number of graphene unit cells and electrically reconfiguring the graphene chemical potential of the RIS is discussed.
- In view of the smart THz wireless communication environment, this paper finally presents a simple RIS-aided communication model to study the impact of the proposed graphene-based RIS on the signal-to-noise ratio (SNR). The results reveal the great potential of the graphene-based RIS at THz band, which can be promising for

intelligent and efficient environment for THz wireless communication.

The remainder of this paper is organized as follows. The material properties of graphene that are important from a RIS design point of view is briefly discussed in Section II. Section III presents the design and equivalent circuit model of a novel graphene-based RIS at THz band, which can actively manipulate the incoming THz wave. In Section IV, the performance of the proposed graphene-based RIS is numerically analyzed. Section V presents the graphene-based RIS-aided THz communication model. Finally, the conclusion is drawn in Section VI.

II. Material Properties of Graphene at THz

Two-dimensional nanomaterial graphene is a monolayer of carbon atoms arranged in a hexagonal lattice. The novel properties of graphene at the THz band open plenty of applications in several fields [34]. At THz frequencies, graphene supports the plasmonic wave propagation, and the surface plasmons possess strong confinement, low loss, and good tunability [35].

The conductivity of graphene is the sum of the conductivity from both interband and intraband transition [36]. The intraband transition governs the conductivity of graphene in the THz frequency regime, which can be approximated as

$$\sigma_s(\omega,\mu_c,\Gamma,T) = -j\frac{e^2 K_B T}{\pi\hbar^2(\omega - j2\Gamma)} \times \left[\frac{\mu_c}{K_B T} + 2\ln\left(\exp\left(-\frac{\mu_c}{K_B T}\right)+1\right)\right], \tag{1}$$

where j is the imaginary unit, T is the temperature, K_B is the Boltzmann's constant, e is the charge of electron, $\hbar$ is the reduced Planck's constant, scattering rate $\Gamma = 1/2\tau$, τ is the relaxation time, ω is the angular frequency, and μ_c is the chemical potential. At the THz band, graphene-based devices are enabled solely by intraband transitions [37]–[39].

The graphene conductivity can be tuned by adjusting the chemical potential μ_c level of the graphene. By using the electric field effect through a bias voltage or chemical doping process, the chemical potential of graphene can be dynamically controlled, thereby enabling the tunable graphene conductivity. Then, the chemical potential in terms of the applied bias voltage V_g can be expressed as [40]

$$\mu_c = \hbar v_f \sqrt{\frac{\pi C V_g}{e}}, \tag{2}$$

where $C = \epsilon_r\epsilon_0/h$ is the electrostatic gate capacitance, ϵ_r is the relative permittivity of substrate, ϵ_0 is the absolute permittivity in free space, h is the height of the substrate, and v_f is Fermi velocity of the graphene. The applied voltage V_g controls the carrier concentration $n \approx CV_g/e$.

The graphene permittivity can be obtained by its conductivity as [41]

$$\epsilon_g = 1 + j\frac{\sigma_s}{t_g\epsilon_0\omega}, \tag{3}$$

where t_g is the graphene thickness.

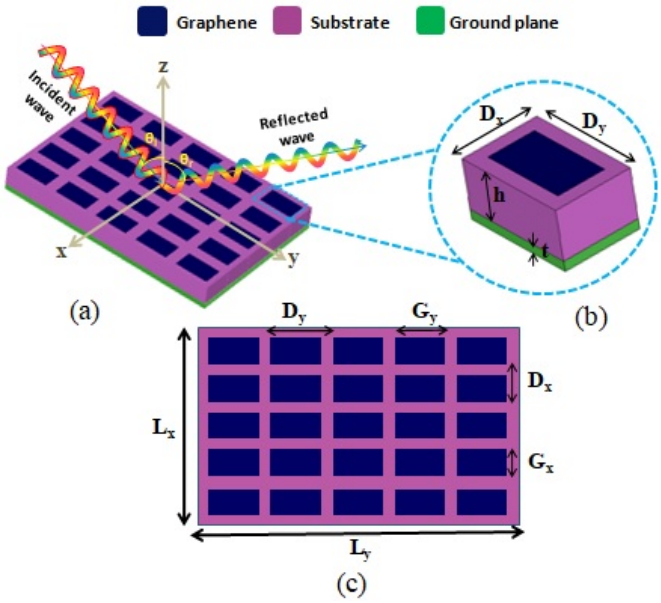

Fig. 1. Schematic of the graphene RIS; (a) 3D view of RIS, (b) unitcell, (c) top view of RIS with geometrical parameters.

From the above equations, we can notice that the conductivity and permittivity of the graphene can be dynamically controlled by an applied bias voltage. This property enables the reconfiguration ability in graphene-based devices.

III. Design and Analysis of Graphene-based THz RIS

A. Design of Graphene RIS

A simple and smart RIS using graphene meta-atoms at the THz band is investigated. The RIS design consists of a 2D periodic array of graphene meta-atoms placed over a metallic grounded silicon substrate. Graphene is modelled as a thin conductive sheet with thickness $t_g = 1$ nm [32]. The proposed graphene-based RIS structure has been simulated in the CST Microwave studio, using a frequency-domain solver with tetrahedral mesh [42]. The number of tetrahedral mesh cells used to simulate the unit structure is 6604. The Floquet port is considered for the excitation of the structure. The Floquet port is positioned around 15.34 μm away from the surface of the structure. Two Floquet modes are excited to study the response of the proposed model. The response of the proposed graphene model is studied in wide spectrum from 0.1 to 4 THz.

In the present work, we consider the room temperature T = 300 K, the Fermi velocity $v_f = 10^6$ m/s and mobility of graphene $\mu_g = 10000$ cm^2/Vs [43]. Graphene RIS is easily reconfigured by applying an external gate voltage V_g via the chemical potential ranging from $\mu_c = 0$ eV to $\mu_c = 0.6$ eV. The relaxation time of graphene is computed as $\tau = \mu_g\mu_c/ev_f^2$. The dimensions of the RIS and the graphene properties are chosen for the active control over reflection, absorption, and anomalous reflection of the THz waves.

Fig. 1 shows the schematic of the proposed graphene-based RIS design and its unit cell. The graphene meta atom is

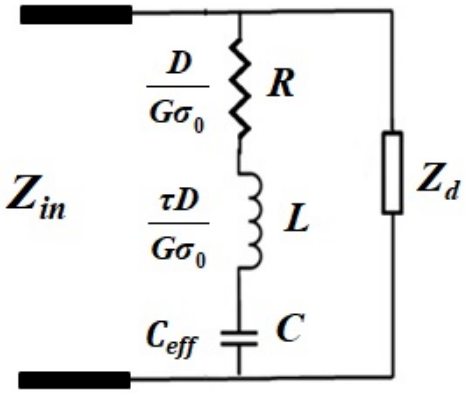

Fig. 2. Equivalent circuit of graphene RIS structure.

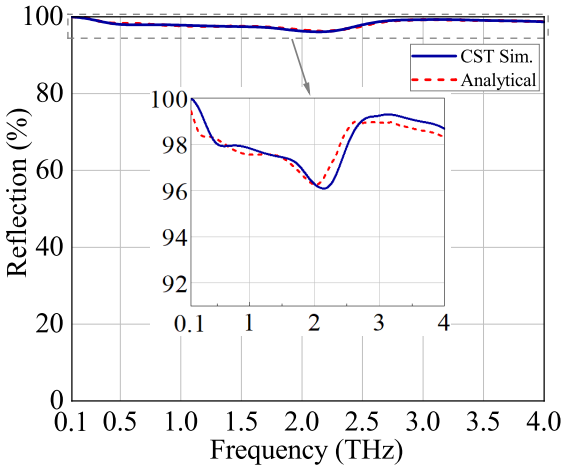

Fig. 3. Reflection spectra of the proposed graphene RIS.

placed over the metal-backed silicon substrate. The graphene-based RIS comprises an array of graphene unit cells with periodicity D_x = 16 μm and D_y = 24 μm along x- and y-axis, respectively. The width and length of the graphene unit cell are G_x = 10 μm and G_y = 18 μm, respectively. The operational frequency is ranging from 0.1 to 4 THz. The substrate thickness is considered as h = 10 μm. The perfect electrical conductor (PEC) is used for ground plane with thickness $t = 1.2$ μm. The proposed graphene-based RIS design attains an ultrathin structure at THz band.

The proposed graphene-based RIS design can be experimentally fabricated in the following way. A silicon wafer sample can be utilized in the mechanical support of graphene-based structure. A silver film can be deposited on the silicon wafer using the electron beam evaporation technique [33]. Then, the silicon dielectric of 10 μm thickness can be deposited on the silver film by using the plasma-enhanced chemical vapour deposition technique. Finally, graphene sheets can be transferred to the silicon dielectric substrate by using electron-beam lithography [44].

B. Circuit Modeling of Graphene RIS

An equivalent circuit model of the proposed graphene-based RIS structure and its closed-form solution is introduced. We study the reflection wave properties of graphene-based THz RIS. A circuit model of the proposed graphene RIS is illustrated in Fig. 2.

The graphene patch is modelled as a thin resistive sheet with the surface impedance $Z_s = 1/\sigma_s$. At the low THz band, the surface conductivity σ_s of the graphene, given by (1), can be expressed in the Drude form as

$$\sigma_s = \frac{\sigma_0}{1 + j\omega\tau}, \tag{4}$$

where

$$\sigma_0 = \frac{e^2 K_B T \tau}{\pi\hbar^2}\left[\frac{\mu_c}{K_B T} + 2\ln\left(\exp\left(-\frac{\mu_c}{K_B T}\right) + 1\right)\right] \tag{5}$$

Moreover, the surface impedance of the array of graphene patches can be expressed as [45]

$$Z_s = \frac{D}{(D-d)\,\sigma_s} - j\frac{\pi}{\omega\epsilon_0\,(\epsilon_r+1)\,D\ln\left(\csc\left(\pi d/2D\right)\right)}, \tag{6}$$

where D is the periodicity in graphene RIS, d is the distance between graphene patches, ϵ_r is the relative permittivity of substrate, and $G = D - d$ is the width of the graphene patch. The above equation can be further written as

$$Z_s = \frac{D}{G\sigma_s} - j\frac{1}{\omega C_{\text{eff}}}, \tag{7}$$

where the effective capacitance

$$C_{\text{eff}} = \frac{1}{\pi}\omega\epsilon_0\,(\epsilon_r+1)\,D\ln\left(\csc\left(\frac{\pi d}{2D}\right)\right),$$

arises from gaps between the graphene patches.

By using the Drude form of the graphene surface conductivity, the surface impedance Z_s of graphene is expressed as

$$Z_s = \frac{D}{G\sigma_0} - j\left[\frac{\omega\tau D}{G\sigma_0} - \frac{1}{\omega C_{\text{eff}}}\right]. \tag{8}$$

From the above equation, the graphene RIS structure can be modelled as a resistor-inductor-capacitor $(R-L-C)$ circuit. The resistance R and the inductance L are due to the graphene patches, and the capacitance C is induced by the gap between the graphene patches. These can be written as

$$R = \frac{D}{G\sigma_0}, L = \frac{\tau D}{G\sigma_0}, \text{and } C = C_{\text{eff}}. \tag{9}$$

The input impedance of the metal-backed substrate can be expressed as

$$Z_d = jZ_c\tan\left(\beta h\right), \tag{10}$$

where Z_c is the characteristic impedance and β is the wave number.

The total impedance of graphene RIS can be expressed as

$$\frac{1}{Z_{in}} = \frac{1}{Z_s} + \frac{1}{Z_d}. \tag{11}$$

Then, the reflection coefficient S_{11} of graphene RIS is

$$S_{11} = \frac{Z_{in} - Z_0}{Z_{in} + Z_0}, \tag{12}$$

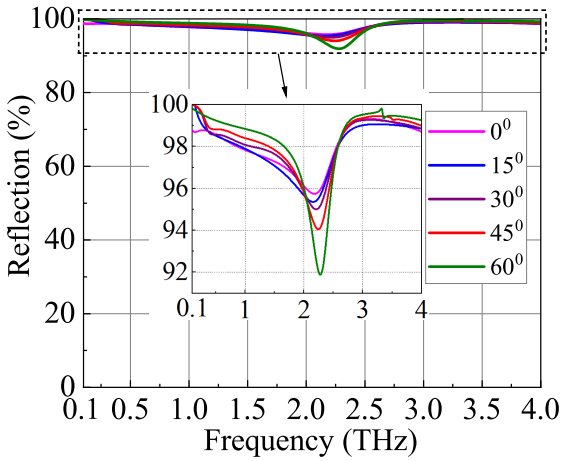

Fig. 4. Reflection spectra of graphene RIS at different angle of incidences from 0^0 to 60^0.

where Z_0 is the free space impedance.

The transmission coefficient is zero due to metallic grounded substrate. Finally, the absorption of the graphene RIS can be expressed as

$$A = 1 - |S_{11}^2|. \tag{13}$$

IV. Results and Analysis

The proposed graphene-based unit cell and RIS design are validated in the EM solver CST Microwave Studio [42]. To excite the impinging plane wave onto the structure, a Floquet port is applied in the EM simulation of graphene unit cell and RIS.

A. Perfect Reflection

Fig. 3 shows the reflection efficiency of the proposed RIS structure. It can be noticed that the proposed graphene RIS provides nearly 100% reflection in a broad frequency regime from 0.1 to 4 THz by appropriate selection of unit cell dimension and graphene material properties. The RIS design attains zero transmission due to the metallic grounded substrate in the structure. A RIS with nearly 100% reflection and zero transmission provides nearly zero absorption.

Fig. 3 further presents the agreement in the results obtained from analytical circuit modeling and 3D EM solver (CST). In the analytical model, the reflection of graphene-based RIS is calculated from (12). In the CST simulation, the graphene is modelled as a monolayer of thickness $t_g = 1$ nm with conductivity σ_s and permittivity ϵ_g, as given in (1) and (3), respectively.

Graphene THz RIS provides more than 96% efficiency of reflection over the operational frequency ranging from 0.1 THz to 4.0 THz. Furthermore, it achieves nearly 100% reflection in operational THz frequency regime at both normal and oblique incidence for both TE and TM polarization, which are discussed in the next sub-sections.

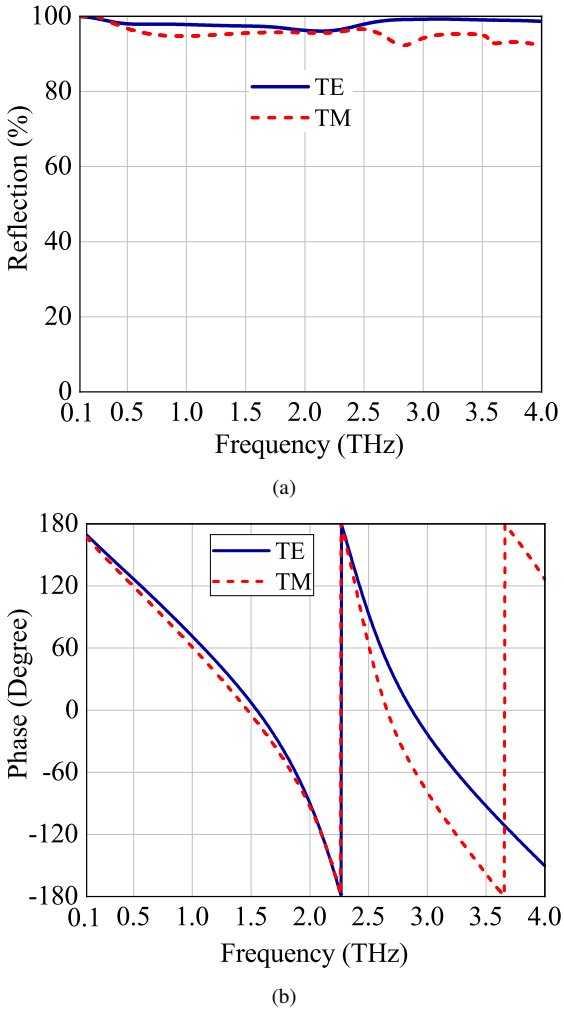

Fig. 5. (a) Reflection, and (b) phase response of graphene RIS at normal incidence for both TE and TM polarization.

(i) At Normal and Oblique Incidence

Fig. 4 shows the reflection efficiency of the graphene RIS at different incidence angles from 0^0 to 60^0. Generally, THz waves incident in different directions and a high reflection efficiency performance at both normal and oblique incidences is significant for real applications. It can be noticed that the high reflection efficiency over the operating frequency regime for normal and oblique incidences is more than 92%.

(ii) Under TE and TM Polarization

In order to investigate the reflection performance in a different state of polarization, we obtain the reflection efficiency for TE and TM polarization under normal and oblique incidences. Fig. 5 shows the reflection efficiency and phase for TE and TM polarization at normal incidence. It can be seen that the graphene-based RIS design is insensitive to polarization. For both cases, the RIS provides more than 90% efficiency of reflection over the operational frequency range from 0.1 THz to 4.0 THz. The phase response for both polarization state is approximately the same from 0.1 to 2.5 THz. Above 2.5 THz, the phase response slightly changes.

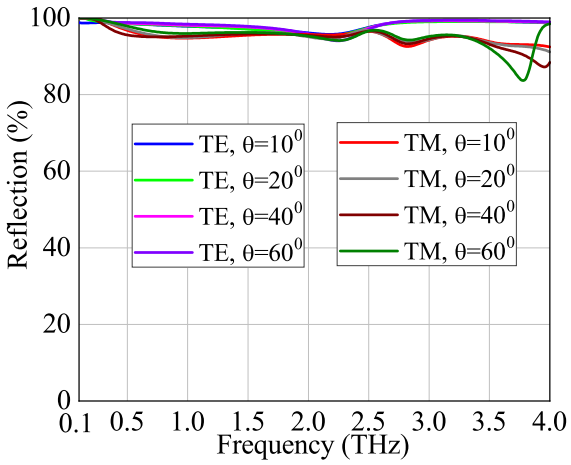

Fig. 6. Reflection of graphene RIS under oblique incidence for both TE and TM polarization.

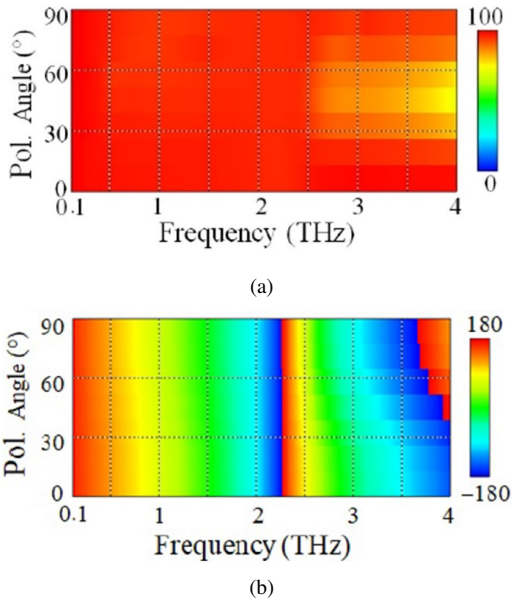

Fig. 7. (a) Reflection, and (b) phase response of graphene RIS for different angles of polarization.

Fig. 6 illustrates the performance of the reflection efficiency for oblique angle of incidences from 10^0 to 60^0 in both TE and TM state of polarization. The high reflection efficiency maintains under oblique incidences in both polarization states. Particularly, it can be noticed from Fig. 6 that the reflection efficiency is more than 95% over the operational frequency from 0.1 to 4 THz for TE mode. However, especially near 4 THz, reflection efficiency slightly reduces with increase of incident angle in the TM mode. The minimum reflection efficiency under oblique incidences for TM mode is 85%.

(iii) At different angle of Polarization

Fig. 7 shows the reflection and phase response of graphene-based RIS for different angles of polarization from 0^0 to 90^0. It can be noticed that nearly 100% reflection efficiency is obtained for all polarization angles ranging from 0^0 to 90^0

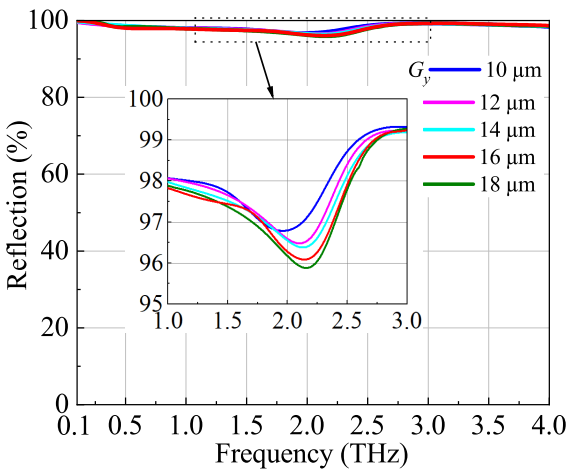

Fig. 8. Reflection of graphene RIS for different lengths of graphene unit cell.

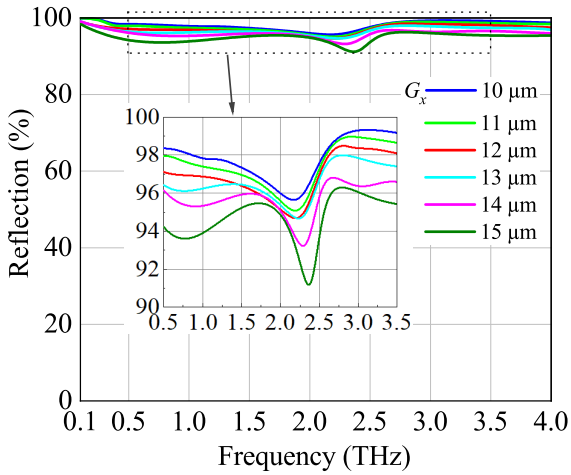

Fig. 9. Reflection of graphene RIS for different widths of graphene unit cell.

in the frequency range 0.1 - 2.5 THz. Above 2.5 THz, the reflection efficiency slightly decreases for polarization angles from 20^0 to 70^0.

(iv) Impact of unit cell's dimensions

The selection of an appropriate dimension of unit cell is significant in achieving excellent performance in RIS. Fig. 8 and Fig. 9 show the reflection performance of the graphene RIS for different length and width of the graphene unit cell. It can be observed from Fig. 8 that a high reflection efficiency is maintained if the length of graphene unit cell is considered from 10 μm to 18 μm. The reflection efficiency decreases, if the length of the graphene unit-cell is more than 18 μm and less than 10 μm. Similarly, high reflection efficiency is maintained, if the width of the graphene unit cell is considered from 10 μm to 15 μm, and decreases for the length of more than 18 μm and less than 10 μm.

(vi) Impact of RIS's Height

The height of the RIS plays a significant role in achieving a better performance. We studied the reflection performance

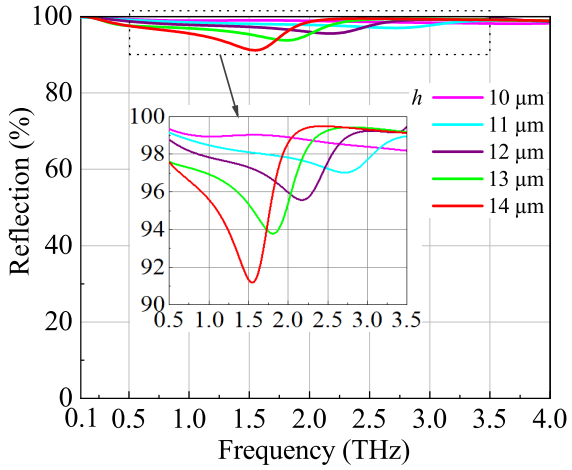

Fig. 10. Reflection for different height of graphene RIS.

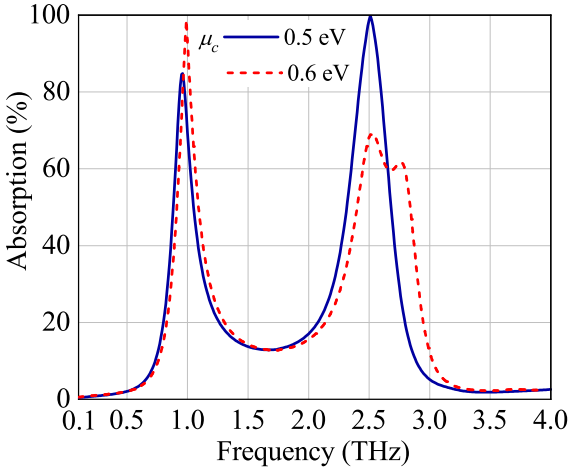

Fig. 11. Perfect absorption of graphene RIS at 1 THz and 2.5 THz.

of the graphene-based RIS for different heights from 10 μm to 14 μm, which is shown in Fig. 10. It can be noticed that more than 90% of the reflection efficiency is achieved, if the height of RIS from 10 μm to 14 μm is considered. More than 98% of the reflection efficiency is attained when the height of 10 μm is considered, and the reflection efficiency gradually decreases when the height increases slightly.

B. Perfect Absorption

Besides the perfect reflection properties, perfect absorption is another significant function of the RIS. Perfect absorption means no reflection and no transmission. We target the perfect absorption in graphene-based RIS by using the electric field effect via graphene chemical potential by applying a bias voltage to the graphene layer. Perfect absorption exhibits under the condition of impedance matching, i.e, when the input impedance of the MSF is matched to the free space impedance $Z_0 = 377\ \Omega$. The tunable chemical potential parameter of graphene is used to match the input impedance of the MSF. Practically tunable graphene chemical potential is achieved by applying the different external voltage to graphene. Perfection absorption ($A = 100\%$) is attained at 1 THz and 2.5 THz

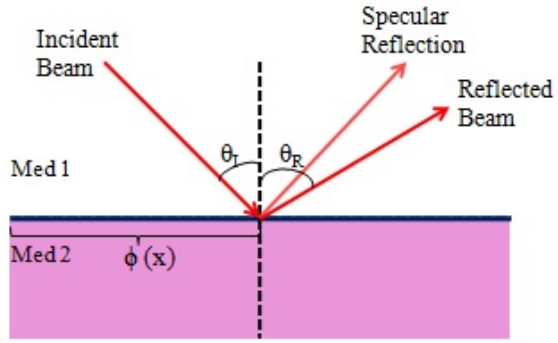

Fig. 12. Conceptual illustration of the anomalous reflection of RIS.

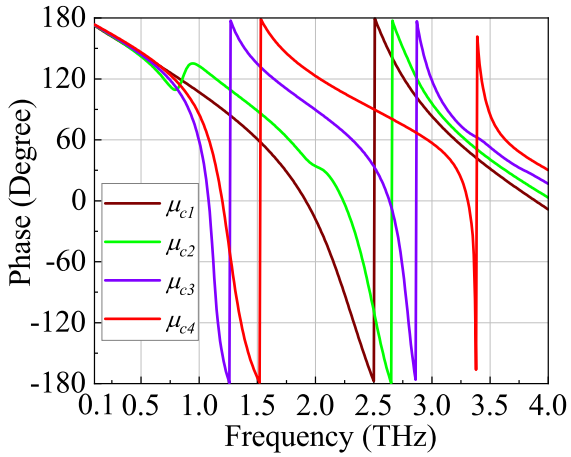

Fig. 13. Phase response at different chemical potentials of graphene.

when the chemical potential of graphene μ_c is equal to 0.6 eV and 0.5 eV respectively, which is shown in Fig. 11. All the incident wave power is absorbed by the RIS at 1 THz and 2.5 THz, since there is no transmission and reflection.

C. Tunable Anomalous Reflection

Anomalous reflection means that the angle of reflection is different from the angle of incidence, i.e, the reflected beam is steered away from the specular reflection beam, as shown in Fig. 12. For anomalous reflection, we need a particular response of several unit cells forming an RIS in order to steer the reflected wave to the desired directions. The beam steering capability of the RIS is mainly controlled by the phase profile of each unit cells that constitute the reflecting surface. It should be noted that the required phase profile achieved by distributing the unit cells with different phase responses can operate well only at a certain frequency. An RIS with a higher reflection efficiency requires the unit cell to have a more extensive phase variation range and higher amplitude response.

According to Huygens principle, each unit can be regarded as a secondary wave source, with different amplitude and phase positions; these secondary wave sources are superimposed on each other to form a reflected wave. By adjusting the amplitude and phase response of the RIS element, the wavefront of the reflected wave can be controlled. In the

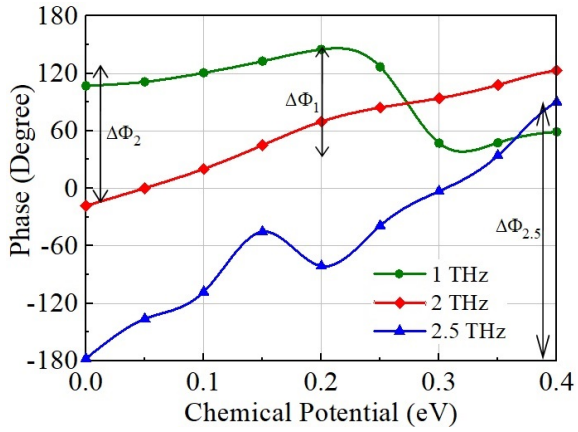

Fig. 14. Phase shift of the graphene unit cell at 1 THz, 2 THz and 2.5 THz.

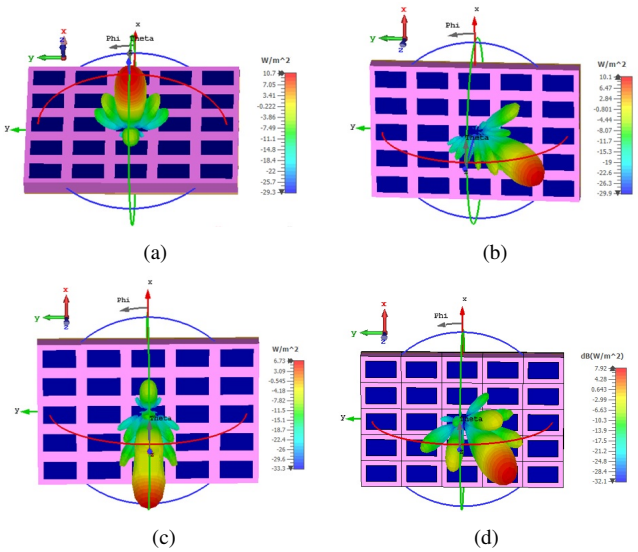

Fig. 15. Beam steering using graphene RIS. (a) $\Phi_1 = 0°$, $\theta_1 = 0°$, (b) $\Phi_2 = 0°$, $\theta_2 = 45°$, (c) $\Phi_5 = 0°$, $\theta_5 = 120°$, (d) $\Phi_6 = 60°$, $\theta_6 = 60°$.

proposed graphene RIS, the dynamic beam control is achieved by adjusting the phase profile of the graphene unit cell of the RIS.

The guidance in determining the required phase profile to steer the beam into a certain direction is the generalized Snell's law [46]. The angle of reflection depends not only on the frequency of the incident wave, the angle of incidence and the refractive index of the incidence medium, but also on the phase gradient of the reflecting surface. The relationship between the incidence and reflection angle is generalized according to Snell's law of reflection [46],

$$n_I \sin\theta_R - n_I \sin\theta_I = \frac{\lambda}{2\pi}\nabla\Phi, \tag{14}$$

where θ_R is the angle of reflection, θ_I is the angle of incidence, and λ is the wavelength of the incident electromagnetic wave, n_I is the refractive index of the incidence medium, and $\nabla\Phi$ is the phase gradient.

In free space with normal incidence ($n_I = 1$, $\theta_I = 0$), the angle of reflection is simplified as

$$\theta_R = \sin^{-1}\left(\frac{\lambda}{2\pi}\nabla\Phi\right). \tag{15}$$

The reflected wave is controlled by the phase gradient of the RIS. With the capability of being electrically tunable, graphene RIS has manifested itself as a promising candidate to attain beam steering. The graphene-based RIS has the capability of dynamically steering the reflection angle in a wide range by electrically reconfiguring the graphene chemical potential.

In the proposed graphene unit cell, the phase response is studied for different chemical potential μ_c of graphene such as $\mu_{c1} = 0$ eV, $\mu_{c2} = 0.12$ eV, $\mu_{c3} = 0.25$ eV, $\mu_{c4} = 0.4$ eV. Large phase variation with the change of chemical potential of graphene is illustrated in Fig. 13. As shown, it can be seen that when the graphene chemical potential changes from 0 to 0.4 eV, the large phase shift of the graphene unit cell can reach up to 270°. It should be marked that the required phase profile achieved by distributing the graphene unit cells with different phase responses can operate well only at a certain frequency. The phase shift for frequency 1 THz, 2 THz and 2.5 THz is depicted in Fig. 14. From this figure, it can be observed that the phase shift for 1 THz, 2 THz and 2.5 THz are $\Delta\Phi_1$ = 98°, $\Delta\Phi_2$ = 141° and $\Delta\Phi_{2.5}$ = 270°, respectively. The graphene RIS can realize a continuous change of the reflected wave into different steering angles, shown in Fig. 15. By designing the phase distribution, which is controlled by the voltage profile, graphene RIS can reflect the wave to the desired direction (θ, Φ), where θ and Φ are the azimuthal angle and the polar angle, respectively. Experimentally, the beam steering principle is based on the gate voltage controlled graphene RIS. The gate voltage V_g is applied to each graphene layer to control the chemical potential of graphene [44].

In order to quantify the beam steering feasibility of the proposed THz RIS, we set the analysis in the antenna array theory formalism, where the array of graphene elements is considered. We obtain the response of graphene RIS in the form of far-field beam steering produced by normal incident plane waves. The far-field radiation pattern F (θ, Φ) can be expressed as

$$F(\theta,\Phi) = f_E(\theta,\Phi) \times AF(\theta,\Phi), \tag{16}$$

where θ and Φ are the elevation angle and the azimuth angle of arbitrary direction, respectively. $f_E(\theta, \Phi)$ is the element (unit cell) radiation pattern function and AF (θ, Φ) is the array factor. For a 2D configuration, the array factor is given as [47],

$$AF(\theta,\Phi) = \sum_{p=1}^{P}\sum_{q=1}^{Q} A_{pq}\exp\left(-j\beta_{pq}\right) \times \exp\left(-jk_0(x_{pq}\sin\theta\cos\Phi + y_{pq}\sin\theta\sin\Phi)\right), \tag{17}$$

where the double summation represents the positions of row and column unit cells of 2D array configuration, P and Q represent the number of elements in row and column respectively, A_{pq} is the amplitude of each element, k_0 is the free space wave number, β_{pq} represents the progressive

TABLE I
DEPENDENCE OF THE REFLECTION ANGLE ON THE NUMBER OF UNIT CELLS AND THE LENGTH OF RIS

Angle of Incidence θ_I (Deg)	**Number of Unit cells** M	**Length of Graphene RIS** L_y (µm)	**Angle of Reflection** θ_R (Deg)
10	56	898	20
	29	458	30
	18	280	45
	13	216	60
	12	189	75
20	59	949	30
	26	410	45
	18	286	60
	15	240	75
30	66	1056	40
	35	563	50
	26	409	60
	21	341	70
	19	309	80
40	76	1209	50
	42	669	60
	32	505	70
	27	438	80

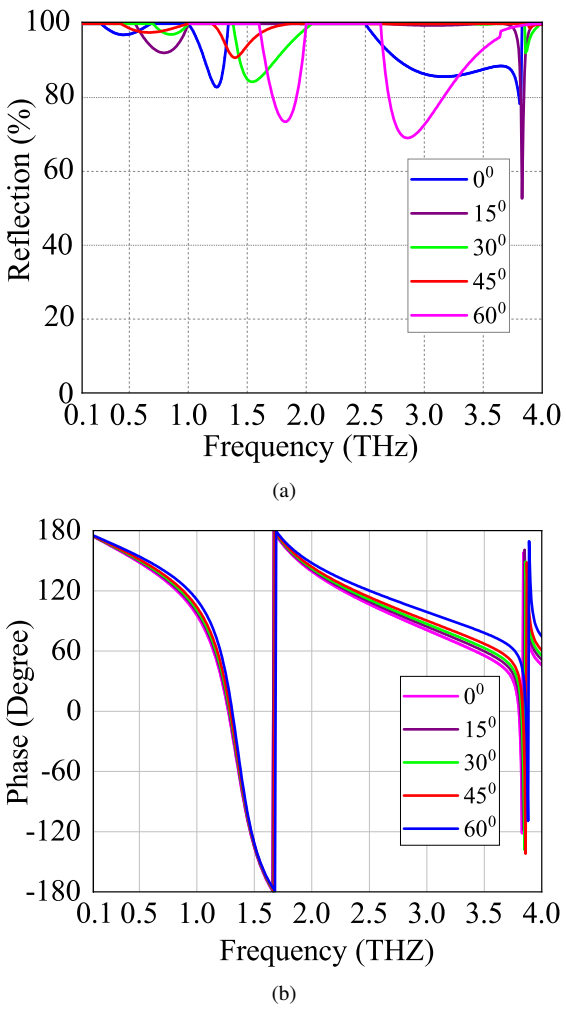

(a)

(b)

Fig. 16. (a) Reflection, and (b) phase response of metallic based RIS at normal and oblique incidence.

phase excitation between the elements, x_{pq} and y_{pq} denote the position of the unit cell along the x-axis and y-axis, respectively. The reflected wave from unit cells of graphene RIS directed at the beam steering angle (θ, Φ). We evaluate the far-field beam steering process of the graphene RIS of 25 unit cells from an electromagnetic perspective. We study the graphene RIS to steer the beam at ($\Phi_1 = 0°$, $\theta_1 = 0°$), ($\theta_2 = 0°$, $\Phi_2 = 45°$), ($\theta_4 = 0°$, $\Phi_4 = 120°$) and ($\theta_4 = 60°$, $\Phi_4 = 60°$). Fig. 15 shows the far-field radiation pattern with graphene RIS geometries. This far-field analysis of graphene RIS is obtained at 2 THz frequency. Sub-wavelength periodic structures and MSF are generally simulated as infinite arrays along with the directions of periodicity by considering a unit cell with the appropriate boundary conditions. This significantly reduces the computational effort for simulation and is a good approximation for most applications. However, all MSF and related structures are necessarily finite. Hence, in Fig 15, we modelled 25 elements of a 5×5 array structure. The appropriate selection of dimension of structure, Floquet port distance and meshing reduces the truncation effect. The truncation effect has a negligible impact on the far-field results of this finite array structure. In the 25 elements periodic array structure, a small increase of sidelobe level is observed. The radiated wave by the RIS exhibits a highly directive beam and directing in the desired beam steering direction. Further, the phase gradient along the y-direction can be expressed as dΦ/dy = $2\pi/L_y$ [48]. Thus, the reflection angle θ_R can be written as

$$\theta_R = \sin^{-1}\left(\sin\theta_I + \frac{\lambda}{L_y}\right). \tag{18}$$

The length L_y of the graphene RIS can be modified by changing the number of unit cell, i.e, $L_y = M \times D_y$. Also, the reflection angle can be controlled by adjusting the number of unit cells, which is presented in Table I. It can be noticed that an RIS of smaller length corresponds to a larger reflection angle.

V. METALLIC-BASED RIS AT THZ BAND

In order to compare the performance of graphene-based RIS with PEC-based RIS, we modelled and analysed a metallic RIS at the THz band. The metallic RIS design consists of a 2D periodic array of conventional metal copper meta-atoms placed over a metallic grounded silicon substrate. The dimension of metallic RIS structure is chosen the same as the proposed graphene–based RIS structure. The operational frequency of

metallic RIS is considered the same as graphene-based RIS, i.e., ranging from 0.1 to 4 THz. Fig. 16 shows the reflection and phase response of the metallic RIS at normal and oblique incidence angles from 0° to 60°. It can be observed that the response of metallic based RIS at both normal and oblique incidences over the operational THz frequency range is inferior in comparison to graphene-based RIS. It can also be noted that the same size and same substrate material are considered for metallic RIS as for graphene-based RIS. The performance of metallic RIS can be improved by appropriate selection of dimension, material and frequency regime.

Metallic-based MSFs can manipulate the propagation of light waves. However, conventional metallic MSFs mainly work efficiently in the optical frequency regime, since it supports the surface plasmon resonance at the optical frequency regime. Metallic-based MSFs also lack sufficient tunability. The plasmonic response of metallic MSFs become less pronounced at the THz band because of the weaker interaction between electromagnetic waves and electrons. This limits the use of noble metals in THz applications.

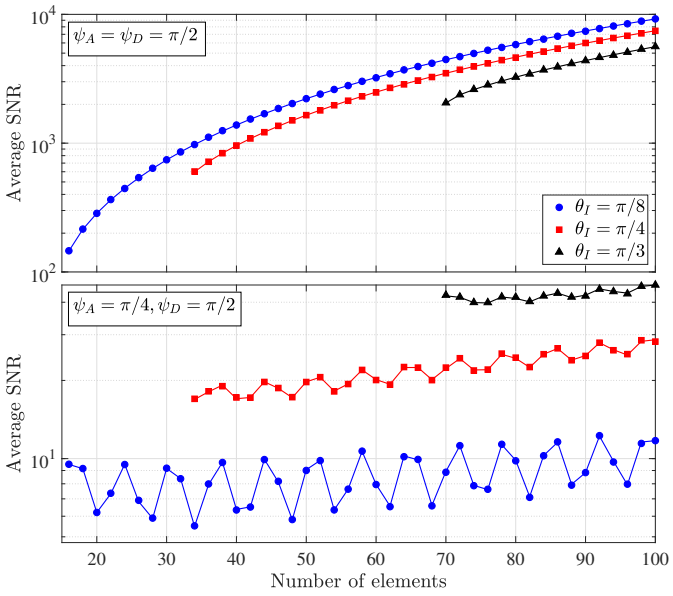

Fig. 17. Average SNR with respect to the number of elements M.

VI. Graphene-based RIS-aided THz Communications

In this section, we consider a simple RIS-aided communication model to study the impact of the proposed graphene-based RIS on the SNR.

A. System Model

We consider a simple topology, where a base station (BS) communicates with a user with the assistance of an RIS. The BS is equipped with a uniform linear array (ULA) of N antennas, the RIS has M reflecting elements (unit cells) arranged in a ULA[1] , whereas the receiver has a single antenna. It is assumed that a direct link between the transmitter and the receiver is not available [49]. Since in THz communications, the line-of-sight (LOS) links are dominant (compared to non-LOS links), the channel matrix between the BS and the RIS is written as

$$\mathbf{H} = \sqrt{NM} g_R \mathbf{a}^H(M, \psi_A)\mathbf{a}(N, \theta_o), \tag{19}$$

where $g_R \in \mathbb{C}$ is the complex channel gain and $\mathbf{a}(N, \theta_o)$ is the array steering vector of the BS given by

$$\mathbf{a}(N, \theta_o) = \frac{1}{\sqrt{N}}\left[1 \; e^{\jmath 2\pi \frac{d}{\lambda}\sin(\theta_o)} \; \cdots \; e^{\jmath 2\pi \frac{d}{\lambda}(N-1)\sin(\theta_o)}\right], \tag{20}$$

where d is the distance between adjacent antenna elements, λ is the wavelength and $\theta_o \in [0, 2\pi)$ is the angle of departure (AoD). The array steering vector $\mathbf{a}^H(M, \psi_A)$ at the RIS, is written similarly to (20), where $\psi_A \in [0, 2\pi)$ is the angle of arrival (AoA). Moreover, the channel vector between the RIS and the user is

$$\mathbf{h} = \sqrt{M} g_U \mathbf{a}(M, \psi_D), \tag{21}$$

where $g_U \in \mathbb{C}$ is the complex channel gain, $\mathbf{a}(M, \psi_D)$ is given by (20) and $\psi_D \in [0, 2\pi)$ is the AoD.

Time is slotted and, at each time slot, the i-th element rotates the phase of the incident signal to an angle $\phi_i \in [0, 2\pi)$. As such, the received signal at the user is

$$y = \sqrt{P}\mathbf{h}\mathbf{\Phi}\mathbf{H}\mathbf{w}^H + n, \tag{22}$$

where P is the transmit power, $n \sim \mathcal{CN}(0, \sigma^2)$ is the additive white Gaussian noise (AWGN) with variance σ^2, and $\mathbf{w}$ is the transmit beamforming at the BS, which we assume to be given by[2] [50]

$$\mathbf{w} = \frac{1}{\sqrt{N}}\left[1 \; e^{\jmath 2\pi \frac{d}{\lambda}\bar{\theta}} \; \cdots \; e^{\jmath 2\pi \frac{d}{\lambda}(N-1)\bar{\theta}}\right], \tag{23}$$

where $\bar{\theta} \in U(-1, 1)$. Finally, $\mathbf{\Phi}$ is the diagonal matrix containing the phase shift variables, written as

$$\mathbf{\Phi} = \text{diag}\left[\beta_1 e^{\jmath\phi_1} \; \beta_2 e^{\jmath\phi_2} \; \cdots \; \beta_M e^{\jmath\phi_M}\right], \tag{24}$$

where $\beta_i \in [0, 1]$ is the reflection amplitude at the i-th RIS element. Based on the above results, we consider $\beta_i = 1, \forall\, i$. Therefore, the user's instantaneous SNR is

$$\gamma = \frac{P|g_R|^2|g_U|^2}{N\sigma^2}\left|\sum_{i=0}^{N-1} e^{b_i}\sum_{k=0}^{M-1} e^{\jmath\phi_k + r_k}\right|^2, \tag{25}$$

where $b_i = \jmath 2\pi \frac{d}{\lambda} i(\sin(\theta_o) - \bar{\theta})$ and $r_k = \jmath 2\pi \frac{d}{\lambda} k(\sin(\psi_D) - \sin(\psi_A))$.

B. Average SNR

In what follows, we analytically derive the average SNR, i.e. $\bar{\gamma} = \mathbb{E}[\gamma]$. Here, we assume that $d = \lambda/2$. Based on the previous section, the maximum reflection angle θ_R of a unit cell is given by (18). Hence, in order for a unit cell to achieve reflection, we must have

[1]Even though we consider a ULA, the results from the previous section can still be captured by this model.

[2]The choice of random beamforming is done for the sake of simplicity, since the focus of this work is mainly on the performance of the RIS elements.

$$\frac{\lambda}{MD_x} < 1 - \sin(\theta_I). \tag{26}$$

This implies that $M > \lambda/((1-\sin(\theta_I))D_x)$. To maximize the received signal, the signals need to be phase aligned with $\phi_k = \pi k(\sin(\psi_D) - \sin(\psi_A))$. This requires

$$\theta_R > \pi(M-1)(\sin(\psi_D) - \sin(\psi_A)), \tag{27}$$

which increases linearly with M when $\psi_D \neq \psi_A$.

In the following proposition, we provide the average SNR when the phase shifts are chosen at random, i.e. $\phi_k \in U(-\theta_R, \theta_R)$. However, the analysis can be easily adapted for other phase shift policies.

Proposition 1. *Let θ_R be the maximum reflection angle of a unit cell. Then, under random phase shifts, the average SNR is*

$$\bar{\gamma} = \frac{P}{\sigma^2}|g_R|^2|g_U|^2\kappa, \tag{28}$$

where

$$\kappa = M + \frac{\sin^2(\theta_R)}{\theta_R^2}\sum_{i\neq k}\cos(\pi(\sin(\psi_D) - \sin(\psi_A))(i-k)). \tag{29}$$

Proof. See Appendix. □

It is clear from the above expression that, due to the random transmit beamforming at the BS, the number of antennas and the AoD do not affect the average SNR. Obviously, $\theta_R = \pi$ results in $\kappa = M$, which corresponds to the lowest achievable average SNR. For a given θ_R, the average SNR is maximized at $\psi_D = \psi_A$. Indeed, for $\theta_R = 0$ we get $\kappa = M^2$, which corresponds to the case where the phases are aligned as described above.

In Fig. 17, we illustrate the average SNR with respect to the number of elements M. The considered parameters are $P = 0$ dB, $\sigma^2 = 1$, $g_R = 1$, and $g_U = 1$. The maximum reflection angle is given by (18) for 2 THz, with a wavelength $\lambda = 150$ μm, periodicity $D_x = 16$ μm and incident angles $\theta_I = \pi/8, \pi/4$, and $\pi/3$. The top sub-figure shows the case where the AoA and AoD of the RIS are equal, in particular, $\psi_A = \psi_D = \pi/2$. In this case, the average SNR increases with the number of elements. A larger incident angle requires more elements in order for the RIS to reflect the received signal, as described above. Moreover, a larger incident signal provides a lower average SNR. Finally, the simulation results (depicted with markers) match our theoretical expression (depicted with lines), which confirms our analysis. The bottom sub-figures shows the case where the AoA and AoD are different. Due to this difference, the SNR fluctuates as the number of elements increases. Furthermore, in this case, the best performance in terms of SNR is provided by the largest value of θ_I.

VII. Conclusion

An efficient and simple structured RIS using graphene meta-atoms to control the incoming THz wave is investigated in this work. An equivalent circuit model and closed-form solution of the proposed graphene-based RIS structure is presented. The THz RIS structure provides nearly 100% reflection of THz wave in an operational frequency ranging from 0.1 to 4 THz. The graphene RIS is insensitive to polarization and incident angle. In addition to perfect reflection, the structure has the potential to provide 100% absorption and anomalous reflection by controlling the chemical potential of graphene. The reflection angle is dynamically steered in a wide range by electrically reconfiguring the graphene RIS and controlling the number of graphene unit cells. Furthermore, the impact of the proposed graphene-based RIS on the SNR is studied using a simple RIS-aided communication model. The great potential of the graphene-based THz RIS is promising for THz wireless communications.

Appendix

The average SNR is $\bar{\gamma} = \mathbb{E}[\gamma]$. Therefore,

$$\begin{aligned}\bar{\gamma} &= \frac{P|g_R|^2|g_U|^2}{N\sigma^2}\mathbb{E}\left[\left|\sum_{i=0}^{N-1}e^{b_i}\sum_{k=0}^{M-1}e^{\jmath\phi_k + r_k}\right|^2\right] \\ &= \frac{P|g_R|^2|g_U|^2}{N\sigma^2}\mathbb{E}\left[\left|\sum_{i=0}^{N-1}e^{b_i}\right|^2\right]\mathbb{E}\left[\left|\sum_{k=0}^{M-1}e^{\jmath\phi_k+r_k}\right|^2\right].\end{aligned} \tag{30}$$

The first expectation can be evaluated as

$$\mathbb{E}\left[\left|\sum_{i=0}^{N-1}e^{b_i}\right|^2\right] = \mathbb{E}\left[\sum_{i=0}^{N-1}|e^{b_i}|^2 + \sum_{i\neq k}e^{b_i - b_k}\right] = N, \tag{31}$$

which follows from $\mathbb{E}[|e^{b_i}|^2] = 1$ and $\mathbb{E}[e^{b_i - b_k}] = 0$. The second expectation can be written as

$$\mathbb{E}\left[\left(\sum_{k=0}^{M-1}\cos(\phi_k + r_k)\right)^2\right] + \mathbb{E}\left[\left(\sum_{k=0}^{M-1}\sin(\phi_k + r_k)\right)^2\right]. \tag{32}$$

In order to derive the above, we need

$$\begin{aligned}\mathbb{E}\left[\cos(\phi_k + r_k)\right] &= \frac{1}{2\theta_R}\int_{-\theta_R}^{\theta_R}\cos(\phi + r_k)d\phi \\ &= \frac{1}{\theta_R}\sin(\theta_R)\cos(r_k),\end{aligned} \tag{33}$$

and

$$\mathbb{E}\left[\cos^2(\phi_k + r_k)\right] = \frac{1}{2}\left(1 + \frac{1}{\theta_R}\sin(\theta_R)\cos(\theta_R)\cos(2r_k)\right). \tag{34}$$

Similarly, we have

$$\mathbb{E}\left[\sin(\phi_k + r_k)\right] = \frac{1}{\theta_R}\sin(\theta_R)\sin(r_k), \tag{35}$$

and

$$\mathbb{E}\left[\sin^2(\phi_k + r_k)\right] = \frac{1}{2}\left(1 - \frac{1}{\theta_R}\sin(\theta_R)\cos(\theta_R)\cos(2r_k)\right). \tag{36}$$

By substituting the above in (32) and after several manipulations, we get (29) and the result follows.

REFERENCES

[1] B. Ferguson and X.-C. Zhang, "Materials for terahertz science and technology," *Nat. Mater.*, vol. 1, pp. 26–33, Sept. 2002.

[2] I. F. Akyildiz, J. M. Jornet, and C. Han, "Teranets: ultra-broadband communication networks in the terahertz band," *IEEE Commun. Mag.*, vol. 21, no. 4, pp. 130–135, Aug. 2014.

[3] H. Tabata, "Application of terahertz wave technology in the biomedical field," *IEEE Transactions on Terahertz Science and Technology*, vol. 5, no. 6, pp. 1146–1153, Nov. 2015.

[4] I. Mehdi, J. Siles, C. P. Chen, and J. M. Jornet, "THz technology for space communications," in *2018 Asia-Pacific Microwave Conference (APMC)*, 2018, pp. 76–78.

[5] J. Federici and L. Moeller, "Review of terahertz and sub terahertz wireless communications," *Journal of Applied Physics*, vol. 107, no. 4, p. 111101, June 2010.

[6] H. T. Chen, A. J. Taylor, and N. Yu, "A review of metasurfaces: Physics and applications," *Reports on Progress in Physics*, vol. 79, p. 076401, June 2016.

[7] J. B. Pendry, D. Schurig, and D. R. Smith, "Controlling electromagnetic fields," *Science*, vol. 312, no. 5781, pp. 1780–1782, June 2006.

[8] X.-F. Zhu and S.-K. Lau, "Perfect anomalous reflection and refraction with binary acoustic metasurfaces," *Journal of Applied Physics*, vol. 126, no. 22, p. 224504, Dec 2019.

[9] X. Wang, J. Ding, B. Zheng, S. An, G. Zhai, and H. Zhang, "Simultaneous realization of anomalous reflection and transmission at two frequencies using bi-functional metasurfaces," *Scientific Reports*, vol. 8, p. 1876, Jan 2018.

[10] W. Zhu, F. Xiao, M. Kang, and M. Premaratne, "Coherent perfect absorption in an all-dielectric metasurface," *Applied Physics Letters*, vol. 108, no. 12, p. 121901, Mar. 2016.

[11] S. Kruk, B. Hopkins, I. I. Kravchenko, A. Miroshnichenko, D. N. Neshev, and Y. S. Kivshar, "Broadband highly efficient dielectric metadevices for polarization control," *APL Photonics*, vol. 1, no. 3, p. 030801, Apr. 2016.

[12] A. Pors and S. I. Bozhevolnyi, "Plasmonic metasurfaces for efficient phase control in reflection," *Opt. Express*, vol. 21, no. 22, pp. 27 438–27 451, Nov 2013.

[13] X. Zhang, R. Deng, F. Yang, C. Jiang, S. Xu, and M. Li, "Metasurface-based ultrathin beam splitter with variable split angle and power distribution," *ACS Photonics*, vol. 5, no. 8, pp. 2997–3002, July 2018.

[14] C. Pfeiffer and A. Grbic, "Metamaterial Huygens' surfaces: Tailoring wave fronts with reflectionless sheets," *Phys. Rev. Lett.*, vol. 110, no. 19, p. 197401, May 2013.

[15] L. Li, Y. Shuang, Q. Ma, H. Li, H. Zhao, M. Wei, C. Liu, C. Hao, C. Qiu, and T. J. Jun, "Intelligent metasurface imager and recognizer," *Light Science and Applications*, vol. 8, no. 1, pp. 97(1–9), Oct 2019.

[16] L. Li and T. Jun, "Electromagnetic reprogrammable coding metasurface holograms," *Nat. Commun.*, vol. 8, no. 1, pp. 197(1–7), Aug 2017.

[17] M. Mirmoosa, G. Ptitcyn, V. Asadchy, and S. Tretyakov, "Time-varying reactive elements for extreme accumulation of electromagnetic energy," *Phys. Rev. Applied*, vol. 11, p. 014024, Jan 2019.

[18] A. L. A. K. Ranaweera, T. S. Pham, H. N. Bui, V. Ngo, and J.-W. Lee, "An active metasurface for field-localizing wireless power transfer using dynamically reconfigurable cavities," *Scientific Reports*, vol. 9, no. 1, p. 11735, Aug 2019.

[19] C. Liaskos, S. Nie, A. Tsioliaridou, A. Pitsillides, S. Ioannidis, and I. Akyildiz, "A new wireless communication paradigm through software-controlled metasurfaces," *IEEE Communications Magazine*, vol. 56, no. 9, pp. 162–169, Sept 2018.

[20] C. Qu, S. Ma, J. Hao, M. Qiu, X. Li, S. Xiao, Z. Miao, N. Dai, Q. He, S. Sun, and L. Zhou, "Tailor the functionalities of metasurfaces based on a complete phase diagram," *Phys. Rev. Lett.*, vol. 115, p. 235503, Dec 2015.

[21] Y. Li, J. Lin, H. Guo, W. Sun, S. Xiao, and L. Zhou, "A tunable metasurface with switchable functionalities: From perfect transparency to perfect absorption," *Advanced Optical Materials*, vol. 8, no. 6, p. 1901548, Jan 2020.

[22] K. B. Letaief, W. Chen, Y. Shi, J. Zhang, and Y. A. Zhang, "The roadmap to 6G: AI empowered wireless networks," *IEEE Commun. Mag.*, vol. 57, no. 8, pp. 84–90, Aug. 2019.

[23] I. F. Akyildiz, A. Kak, and S. Nie, "6g and beyond: The future of wireless communications systems," *IEEE Access*, vol. 8, pp. 133 995–134 030, July 2020.

[24] H.-H. Hsiao, C. H. Chu, and D. P. Tsai, "Fundamentals and applications of metasurfaces," *Small Methods*, vol. 1, no. 4, p. 1600064, Mar 2017.

[25] C. Huang, S. Hu, G. C. Alexandropoulos, A. Zappone, C. Yuen, R. Zhang, M. D. Renzo, and M. Debbah, "Holographic mimo surfaces for 6g wireless networks: Opportunities, challenges, and trends," *IEEE Wireless Communications*, vol. 27, no. 5, pp. 118–125, Oct 2020.

[26] S. Dash, A. Patnaik, and B. K. Kaushik, "Performance enhancement of graphene plasmonic nanoantenna for THz communication," *IET Microwaves Antennas Propag.*, vol. 13, no. 1, pp. 71–75, Jan. 2019.

[27] S. Dash, G. Soni, A. Patnaik, C. Liaskos, I. F. Akyildiz, and A. Pitsillides, "Switched-beam graphene plasmonic nanoantenna in the terahertz wave region," *Plasmonics*, vol. 16, pp. 1855–1864, Apr 2021.

[28] Z. Xu, X. Dong, and J. Bornemann, "Design of a reconfigurable MIMO system for THz communications based on graphene antennas," *IEEE Transactions on Terahertz Science and Technology*, June 2014.

[29] S. Dash, C. Liaskos, I. F. Akyildiz, and A. Pitsillides, "Wideband perfect absorption polarization insensitive reconfigurable graphene metasurface for THz wireless environment," in *Proc. IEEE Microwave Theory and Techniques in Wireless Communications (MTTW)*, Oct. 2019, pp. 93–96.

[30] S. Barzegar-Parizi and A. Khavasi, "Designing dual-band absorbers by graphene/metallic metasurfaces," *IEEE Journal of Quantum Electronics*, vol. 55, no. 2, pp. 1–8, Apr 2019.

[31] P. Chen and A. Alu, "Terahertz metamaterial devices based on graphene nanostructures," *IEEE Transactions on Terahertz Science and Technology*, vol. 3, no. 6, pp. 748–756, Nov. 2013.

[32] S. Thongrattanasiri, F. H. L. Koppens., and F. Javier, "Complete optical absorption in periodically patterned graphene," *Phys. Rev. Lett.*, vol. 108, no. 4, p. 047401, Jan. 2012.

[33] A. C. Tasolamprou, A. D. Koulouklidis, C. Daskalak, C. P. Mavidis, G. Kenanakis, G. Deligeorgis, Z. Viskadourakis, P. Kuzhir, S. Tzortzakis, M. Kafesaki, E. N. Economou, and C. M. Soukoulis, "Experimental demonstration of ultrafast THz modulation in a graphene-based thin film absorber through negative photoinduced conductivity," *ACS Photonics*, vol. 6, no. 3, pp. 720–727, Feb. 2019.

[34] A. K. Geim and K. S. Novoselov, "The rise of graphene," *Nature Materials*, vol. 6, no. 3, pp. 183–191, Mar. 2007.

[35] F. H. L. Koppens, D. E. Chang, and F. J. Abajo, "Graphene plasmonics: A platform for strong light-matter interactions," *Nano Lett.*, vol. 11, no. 8, pp. 3370–3377, July 2011.

[36] V. Gusynin, S. G. Sharapov, and J. P. Carbotte, "Magneto-optical conductivity in graphene," *J. Phys.: Cond. Matter*, vol. 19, no. 2, p. 026222, Dec. 2006.

[37] B. Sensale-Rodriguez, R. Yan, M. M. Kelly, T. Fang, K. Tahy, W. S. Hwang, D. Jena, L. Liu, and H. G. Xing, "Broadband graphene terahertz modulators enabled by intraband transitions," *Nature Communications*, vol. 3, no. 1, p. 780, Apr 2012.

[38] A. Andryieuski and A. V. Lavrinenko, "Graphene metamaterials based tunable terahertz absorber: effective surface conductivity approach," *Opt. Express*, vol. 21, no. 7, pp. 9144–9155, Apr 2013.

[39] N. Kakenov, O. Balci, T. Takan, V. A. Ozkan, H. Altan, and C. Kocabas, "Observation of gate-tunable coherent perfect absorption of terahertz radiation in graphene," *ACS Photonics*, vol. 3, no. 9, pp. 1531–1535, 2016.

[40] J. S. Gomez-Diaz. and J. Perruisseau-Carrier, "Graphene-based plasmonic switches at near infrared frequencies," *Optics Express*, vol. 21, no. 13, pp. 15 490–15 504, Jul 2013.

[41] A. Vakil and N. Engheta, "Transformation optics using graphene," *Science*, vol. 332, no. 6035, p. 1291–1294, June 2011.

[42] CST - Computer Simulation Technology Studio Suite Student edition 2020 version.

[43] K. S. Novoselov, A. K. Geim, S. V. Morozov, D. Jiang, Y. Zhang, S. V. Dubonos, I. V. Grigorieva, and A. A. Firsov, "Electric field effect in atomically thin carbon films," vol. 306, no. 5696, pp. 666–669, Oct. 2004.

[44] L. Ju, B. Geng, J. Horng, C. Girit, M. Martin, Z. Hao, H. A. Bechtel, X. Liang, A. Zettl, Y. R. Shen, and F. Wang, "Graphene plasmonics for tunable terahertz tetamaterials," *Nat.Nanotechnol.*, vol. 6, no. 10, pp. 630–634, Sept. 2011.

[45] Y. R. Padooru, A. B. Yakovlev, C. S. R. Kaipa, G. W. Hanson, F. Medina, and F. Mesa, "Dual capacitive-inductive nature of periodic graphene patches: Transmission characteristics at low-terahertz frequencies," *Phys. Rev. B*, vol. 87, no. 11, p. 115401, Mar 2013.

[46] S. Sun, K. Y. Yang, C. Wang, T. Juan, W. T. Chen, C. Y. Liao, Q. He, S. Xiao, W. Kung, G. Guo, L. Zhou, and D. P. Tsai, "High-efficiency broadband anomolous reflection by gradient meta-surfaces," *Nano Lett.*, vol. 12, no. 12, pp. 6223–6229, Nov. 2012.

[47] C. A. Balanis, *Antenna Theory: Analysis and Design*, 4th ed. Wiley, 2016.

[48] J. Zang, D. Correas-Serrano, J. Do, X. Liu, A. Alvarez-Melcon, and J. Gomez-Diaz, "Nonreciprocal wavefront engineering with time-modulated gradient metasurfaces," *Phys. Rev. Applied*, vol. 11, p. 054054, May 2019.

[49] Y. Zhu, G. Zheng, and K. K. Wong, "Stochastic geometry analysis of large intelligent surface-assisted millimeter wave networks," *IEEE Journal on Selected Areas in Communications*, vol. 38, no. 8, pp. 1749–1762, Aug. 2020.

[50] G. Lee, Y. Sung, and M. Kountouris, "On the performance of random beamforming in sparse millimeter wave channels," *IEEE Journal of Selected Topics in Signal Processing*, vol. 10, no. 3, pp. 560–575, Apr. 2016.